

# Gravitational-wave imprints of Kerr–Bertotti–Robinson black holes: frequency blue-shift and waveform dephasing

Xiang-Qian Li,<sup>1,\*</sup> Hao-Peng Yan,<sup>1,†</sup> and Xiao-Jun Yue<sup>1,‡</sup>

<sup>1</sup>*College of Physics and Optoelectronic Engineering,  
Taiyuan University of Technology, Taiyuan 030024, China*

(Dated: December 3, 2025)

We investigate the orbital dynamics and gravitational-wave signatures of extreme mass-ratio inspirals (EMRIs) in the spacetime of a Kerr black hole immersed in an asymptotically uniform magnetic field, described by the exact Kerr–Bertotti–Robinson (Kerr–BR) solution [1]. In contrast to the widely used Kerr–Melvin metric, the Kerr–BR spacetime is of algebraic type D, admits a clear asymptotic structure, and allows for a systematic analytic treatment of geodesics. By analyzing the innermost stable circular orbit (ISCO), we find that the external magnetic field consistently pushes the ISCO to larger radii  $r_{\text{ISCO}}$  for all spin configurations considered. Counterintuitively, despite this outward radial shift, the ISCO orbital frequency  $\Omega_{\text{ISCO}}$  increases monotonically with the magnetic-field strength, leading to a robust “blue-shift” of the gravitational-wave cutoff frequency. We further show that retrograde orbits are significantly more sensitive to magnetic fields than prograde orbits, and identify a frequency crossover phenomenon in which magnetic corrections can invert the usual spin–frequency hierarchy at the ISCO. Finally, employing a semi-analytic adiabatic evolution scheme driven by exact geodesic relations and a leading-order quadrupole flux, we generate inspiral waveforms and quantify the substantial dephasing induced by the magnetic field. Our results indicate that large-scale magnetic environments can leave observable imprints in EMRI signals for future space-based detectors such as LISA, TianQin, and Taiji, and that neglecting such effects in waveform models may introduce non-negligible biases in parameter estimation, particularly for the black-hole spin.

## I. INTRODUCTION

The detection of gravitational waves by the LIGO–Virgo–KAGRA collaboration [2–4] and the imaging of supermassive black holes by the Event Horizon Telescope [5, 6] have ushered in an era of precision gravity. While the Kerr metric [7] remains the standard paradigm for describing astrophysical black holes, it strictly represents a vacuum solution. In realistic astrophysical scenarios, however, black holes are inevitably embedded in nontrivial energetic environments. To capture these effects, extensive theoretical efforts have been devoted to constructing exact or approximate solutions of black holes coupled to various matter–energy distributions. Examples include quintessence-like [8] and Chaplygin-like [9–11] phenomenological cosmological fluids, topological defects such as string clouds [12] and global monopoles [13], as well as scalar fields or boson clouds [14, 15] capable of triggering superradiant instabilities. Among these diverse environmental factors, large-scale magnetic fields are of particular astrophysical relevance due to their ubiquity in accretion flows and their crucial role in jet formation mechanisms. Consequently, understanding how such magnetic environments modify the spacetime geometry and the resulting observables is essential for testing general relativity in the strong-field regime.

Historically, the study of magnetized black holes has largely relied on the Kerr–Melvin solution [16–18], generated via the Harrison transformation. While this spacetime has been extensively used, it exhibits interpretational subtleties, particularly regarding its asymptotic behavior: the magnetic field does not decay at infinity, leading to a Melvin-like rather than asymptotically flat exterior and complicating the standard notion of an asymptotic region and associated conserved quantities. More recently, Podolský and Ovcharenko constructed a new class of exact solutions to the Einstein–Maxwell equations, among which the Kerr–Bertotti–Robinson (Kerr–BR) black hole describes a rotating black hole immersed in an asymptotically uniform magnetic field aligned with the rotation axis [1]. Crucially, unlike the Kerr–Melvin solution, which is of algebraic type I, the Kerr–BR spacetime retains Petrov type D [19, 20]. This algebraic property is of paramount importance, as it implies the existence of hidden symmetries that facilitate the separability of field equations and geodesic motion [21].

Since its proposal, the Kerr–BR metric has garnered significant attention as a testbed for various astrophysical phenomena. Its optical characteristics have been extensively mapped. Wang *et al.* derived approximate analytical expressions for the photon sphere and investigated the black-hole shadow, quantifying deviations from the Kerr case [22]. These shadow features were further explored by Ali and Ghosh, who demonstrated that the magnetic deformation enlarges the shadow and modifies its oblateness, offering a potential avenue for parameter estimation [23]. Complementary studies of the optical

\* lixiangqian@tyut.edu.cn

† yanhaopeng@tyut.edu.cn

‡ yuexiaojun@tyut.edu.cn

properties [24] and strong-field gravitational lensing [25] have shown that the magnetic parameter leaves distinct imprints on lensing observables, such as image positions and time delays. Beyond geometric optics, the thermodynamic and energetic properties of Kerr–BR black holes have also been scrutinized. Zeng and Wang analyzed energy extraction via magnetic reconnection, finding that while the magnetic field generally impedes extraction efficiency compared to the vacuum Kerr case, it still allows for more efficient extraction than in the Kerr–Melvin background [26]. Theoretical extensions of the metric have also been proposed, including superpositions with Bonnor–Melvin fields [27], couplings to nonlinear electrodynamics [28], and the inclusion of string clouds [29]. Potential applications to high-energy astrophysical events, such as short gamma-ray bursts powered by magnetized mergers, have likewise been suggested [30].

The orbital dynamics of test particles, which are central to the modeling of extreme mass-ratio inspiral (EMRI) waveforms, have recently seen rigorous development in this background. Zhang and Wei analyzed the kinematics of spinning test particles, revealing that the magnetic field necessitates increased orbital angular momentum to maintain stability [31]. Most relevant to the present work, Wang derived exact, closed-form expressions for the innermost stable circular orbit (ISCO) radii and analytic inspiral trajectories for uncharged particles in the Kerr–BR spacetime [32]. While Wang’s work provided the foundational geodesic integration, the specific implications of these modified trajectories for gravitational-wave generation—particularly for the frequency evolution and phase accumulation of EMRIs—remain to be fully quantified.

In this paper, we bridge the gap between the exact mathematical solutions of the Kerr–BR geodesic equations and their direct observables in gravitational-wave astronomy. Building upon the exact ISCO relations derived in Ref. [32], we compute the adiabatic evolution of EMRIs in this magnetized background. We show that the presence of the external magnetic field robustly shifts the ISCO frequency to higher values and induces significant dephasing in the emitted waveforms, providing a distinctive observational signature of environmental effects in future space-based gravitational-wave observations.

## II. THE KERR–BERTOTTI–ROBINSON METRIC

The Kerr–Bertotti–Robinson (Kerr–BR) metric describes a rotating black hole of mass  $m$  and spin parameter  $a$  immersed in an external magnetic field characterized by the parameter  $B$ . In coordinates adapted to its

algebraic structure, the line element reads [1]

$$ds^2 = \frac{1}{\Omega^2} \left[ -\frac{Q}{\rho^2} (dt - a \sin^2 \theta d\varphi)^2 + \frac{\rho^2}{Q} dr^2 + \frac{\rho^2}{P} d\theta^2 + \frac{P}{\rho^2} \sin^2 \theta (adt - (r^2 + a^2)d\varphi)^2 \right], \quad (1)$$

where the metric functions are given by

$$\rho^2 = r^2 + a^2 \cos^2 \theta, \quad (2a)$$

$$P = 1 + B^2 \left( m^2 \frac{I_2}{I_1^2} - a^2 \right) \cos^2 \theta, \quad (2b)$$

$$Q = (1 + B^2 r^2) \Delta, \quad (2c)$$

$$\Omega^2 = (1 + B^2 r^2) - B^2 \Delta \cos^2 \theta, \quad (2d)$$

with the modified horizon function  $\Delta$  and auxiliary constants  $I_1, I_2$  defined as

$$\Delta = \left( 1 - B^2 m^2 \frac{I_2}{I_1^2} \right) r^2 - 2m \frac{I_2}{I_1} r + a^2, \quad (3)$$

$$I_1 = 1 - \frac{1}{2} B^2 a^2, \quad I_2 = 1 - B^2 a^2. \quad (4)$$

Here, the factor  $\Omega^2$  plays the role of a conformal factor. In the limit  $B = 0$ , we have  $I_1 = I_2 = 1$ ,  $\Omega^2 = 1$ , and the metric reduces exactly to the standard Kerr solution in Boyer–Lindquist coordinates. In contrast, for  $m = 0$  it reduces to the Bertotti–Robinson universe, a direct-product Einstein–Maxwell solution with a uniform electromagnetic field.

## III. GEODESIC MOTION AND ANALYTICAL RELATIONS

We consider the orbital dynamics of a test particle with rest mass  $\mu$  confined to the equatorial plane ( $\theta = \pi/2$ ). The nonvanishing metric components of the Kerr–BR spacetime [Eq. (1)] on this plane take the compact form

$$g_{tt} = -\frac{1}{\Lambda} \left( \frac{\Lambda \Delta}{r^2} - \frac{a^2}{r^2} \right), \quad (5a)$$

$$g_{t\phi} = \frac{1}{\Lambda} \left( \frac{a \Lambda \Delta}{r^2} - \frac{a(r^2 + a^2)}{r^2} \right), \quad (5b)$$

$$g_{\phi\phi} = \frac{1}{\Lambda} \left( \frac{(r^2 + a^2)^2}{r^2} - \frac{a^2 \Lambda \Delta}{r^2} \right), \quad (5c)$$

where  $\Lambda(r) \equiv 1 + B^2 r^2$  is the conformal factor restricted to the equatorial plane, and  $\Delta(r)$  is the modified horizon function defined in Eq. (3).

### A. Analytical solution for the ISCO radius

The dynamics of the inspiral are bounded by the innermost stable circular orbit (ISCO). Recently, Wang [32]

derived an exact analytical solution for the ISCO radius in the Kerr–BR spacetime. Remarkably, when expressed in terms of the outer and inner horizon radii  $r_{\pm}$  (the roots of  $\Delta(r) = 0$ ), the ISCO radius  $r_{\text{ISCO}}$  takes a form formally identical to the standard Kerr case:

$$r_{\text{ISCO}} = \frac{r_+ + r_-}{2} \left[ 3 + Z_2 \mp \sqrt{(3 - Z_1)(3 + Z_1 + 2Z_2)} \right], \quad (6)$$

where the upper (lower) sign corresponds to prograde (retrograde) orbits. The auxiliary functions are defined as

$$Z_1 = 1 + (1 - \lambda^2)^{1/3} \left[ (1 + \lambda)^{1/3} + (1 - \lambda)^{1/3} \right], \quad (7a)$$

$$Z_2 = \sqrt{3\lambda^2 + Z_1^2}, \quad (7b)$$

$$\lambda = \frac{2\sqrt{r_+ r_-}}{r_+ + r_-}. \quad (7c)$$

Equation (6) provides the precise termination point for our inspiral evolution.

### B. General circular orbits and frequency

To describe the adiabatic evolution *before* reaching the ISCO, we require the orbital frequency  $\Omega_\phi$  and conserved quantities  $(\mathcal{E}, \mathcal{L})$  for general circular orbits at any radius  $r > r_{\text{ISCO}}$ .

The orbital frequency  $\Omega_\phi = d\phi/dt$  is determined by the extremum condition of the effective potential,  $\partial_r V_{\text{eff}} = 0$ . For a generic stationary and axisymmetric spacetime, this condition yields a closed-form expression in terms of the radial derivatives of the metric components ( $g'_{\mu\nu} \equiv \partial_r g_{\mu\nu}$ ) [33]:

$$\Omega_\phi(r; B) = \frac{-g'_{t\phi} + \sqrt{(g'_{t\phi})^2 - g'_{tt} g'_{\phi\phi}}}{g'_{\phi\phi}}. \quad (8)$$

This relation thus gives the exact Keplerian frequency for equatorial circular geodesics in the magnetized background. By substituting Eqs. (5) into Eq. (8), we obtain the precise frequency evolution used in our waveform modeling. In the limit  $B \rightarrow 0$ , Eq. (8) reduces to the familiar Kerr expression  $\Omega_\phi = \sqrt{m}/(r^{3/2} + a\sqrt{m})$ .

The corresponding specific energy  $\mathcal{E}$  and angular momentum  $\mathcal{L}$  for circular orbits follow from the normalization condition  $u^\mu u_\mu = -1$ :

$$\mathcal{E} = -\frac{g_{tt} + \Omega_\phi g_{t\phi}}{\mathcal{N}}, \quad \mathcal{L} = \frac{g_{t\phi} + \Omega_\phi g_{\phi\phi}}{\mathcal{N}}, \quad (9)$$

where the normalization factor  $\mathcal{N}$  is defined as

$$\mathcal{N} = \sqrt{-\left( g_{tt} + 2\Omega_\phi g_{t\phi} + \Omega_\phi^2 g_{\phi\phi} \right)}. \quad (10)$$

The effective potential  $V_{\text{eff}}(r)$  governing the radial motion for a particle with fixed  $\mathcal{E}$  and  $\mathcal{L}$  can then be written

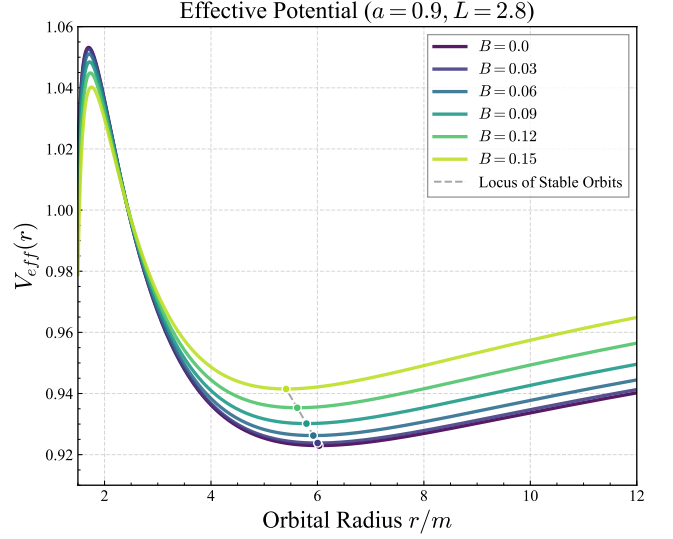


FIG. 1. **Effective potential wells.** The effective potential  $V_{\text{eff}}(r)$  for a test particle with fixed angular momentum  $\mathcal{L} = 2.8$  around a Kerr–BR black hole with  $a = 0.9$ . The colored dots mark the locations of stable circular orbits, and the dashed line indicates the locus of these minima as the magnetic field  $B$  increases. Note that for fixed  $\mathcal{L}$ , the position of the potential minimum shifts inward as  $B$  increases. The ISCO, however, is defined by the onset of marginal stability  $\partial_r^2 V_{\text{eff}} = 0$ ; its behavior as a function of  $B$  is discussed in Sec. IV.

as

$$V_{\text{eff}}(r; B) = -1 + \frac{\mathcal{E}^2 g_{\phi\phi} + 2\mathcal{E}\mathcal{L}g_{t\phi} + \mathcal{L}^2 g_{tt}}{g_{t\phi}^2 - g_{tt}g_{\phi\phi}}. \quad (11)$$

Figure 1 illustrates the behavior of the effective potential for a fixed angular momentum  $\mathcal{L} = 2.8$ . As the magnetic field  $B$  increases, the potential well deepens and its minimum shifts towards smaller radii, indicating enhanced confinement for particles with fixed  $\mathcal{L}$ .

## IV. ISCO SHIFT AND FREQUENCY ANALYSIS

We numerically solve the ISCO conditions for a range of magnetic field strengths  $B$  and spin parameters  $a$ . Our results reveal a robust yet counterintuitive behavior of magnetized black holes.

### A. Outward shift of the stability limit

In Fig. 2, we present the normalized ISCO radius  $r_{\text{ISCO}}(B)/r_{\text{ISCO}}(0)$  as a function of the magnetic field parameter  $B$ . We examine three representative cases: prograde ( $a = 0.9$ ), Schwarzschild ( $a = 0$ ), and retrograde ( $a = -0.9$ ).

A key finding is that the magnetic field systematically increases the ISCO radius,  $r_{\text{ISCO}}(B) > r_{\text{ISCO}}(0)$ , across

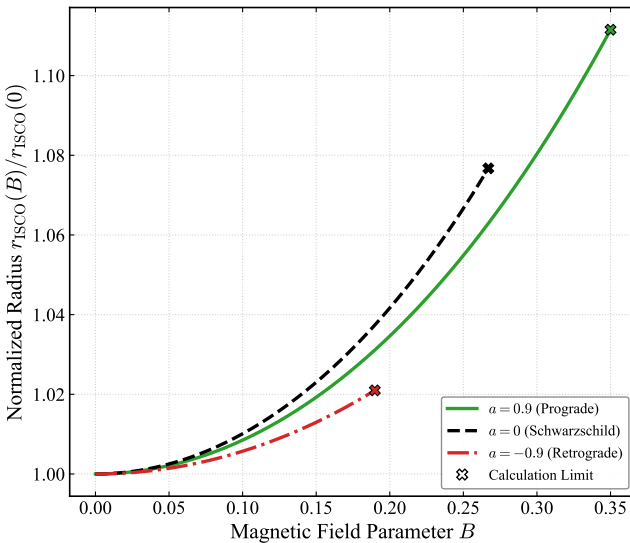


FIG. 2. **Outward shift of the ISCO.** The normalized ISCO radius  $r_{\text{ISCO}}(B)/r_{\text{ISCO}}(0)$  as a function of the magnetic field parameter  $B$ . For all spin orientations, the magnetic field pushes the ISCO to larger radii. The slope shows that retrograde orbits (red dash-dotted line) are dynamically more sensitive to the magnetic field than prograde orbits (green solid line). The ‘X’ markers denote the calculation limit, beyond which the parameters leave the physical regime of the Kerr–BR metric (e.g., loss of a regular event horizon).

all spin configurations sampled. This indicates that the uniform magnetic field provides additional radial support that destabilizes the innermost circular orbits and pushes the marginal stability limit outward. The relative shift is most pronounced for the retrograde case, reflecting a stronger interplay between the magnetic-field-induced curvature corrections and the counter-rotating frame dragging.

### B. Frequency blue-shift and crossover

Standard intuition from Keplerian dynamics suggests that an orbital expansion leads to a decrease in frequency,  $\Omega \sim r^{-3/2}$ . In the Kerr–BR spacetime, however, we find the opposite trend at the ISCO.

As shown in Fig. 3, the ISCO orbital frequency  $m\Omega_{\text{ISCO}}$  monotonically *increases* with the magnetic field strength for all spins considered. This “frequency blue-shift” implies that the magnetic-field-induced curvature corrections in the Kerr–BR metric force the particle to orbit faster in order to maintain a circular geodesic at the outwardly shifted ISCO. The inset in Fig. 3 confirms that even for high-spin prograde orbits ( $a = 0.9$ ), where the vacuum frequency is already high, the magnetic field induces a further blue-shift.

Most remarkably, we observe a generic “crossover” phenomenon. Orbits corresponding to lower spins, which initially have lower ISCO frequencies at  $B = 0$ , exhibit

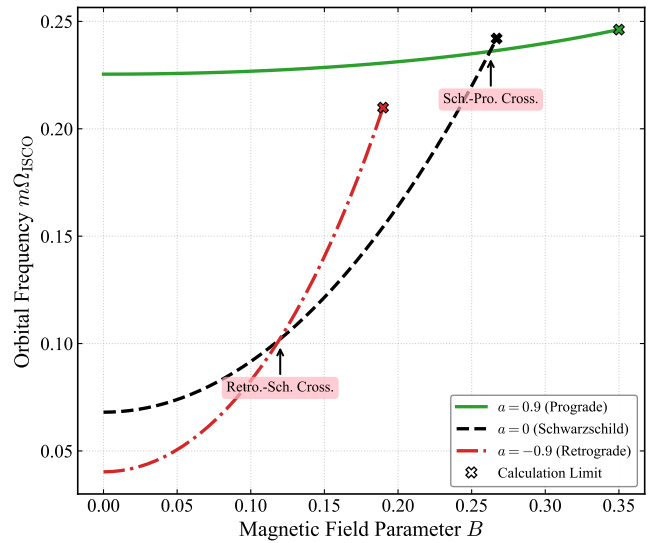


FIG. 3. **Frequency blue-shift and crossover.** The orbital frequency at the ISCO as a function of  $B$ . Despite the increase in ISCO radius, the frequency increases for all spin values (blue-shift). Two distinct crossover events are observed: first at  $B \approx 0.12$ , where the retrograde frequency ( $a = -0.9$ ) exceeds the Schwarzschild case ( $a = 0$ ); and second at  $B \approx 0.26$ , where the Schwarzschild frequency overtakes the prograde orbit ( $a = 0.9$ ). These crossings demonstrate that sufficiently strong magnetic fields can invert the frequency hierarchy typically imposed by the black-hole spin.

a much steeper rise in frequency as  $B$  increases, eventually overtaking the frequencies of higher-spin orbits. For instance, the retrograde orbit ( $a = -0.9$ ) surpasses the Schwarzschild case ( $a = 0$ ) at  $B \approx 0.12$ , and at larger  $B$  the Schwarzschild ISCO frequency can exceed that of the high-spin prograde orbit ( $a = 0.9$ ). Thus, beyond a certain field strength the magnetic corrections override the usual spin-imposed ordering of ISCO frequencies.

This counterintuitive behavior and the crossover phenomenon can be understood by examining how the magnetic field couples to the orbital radius. In the Kerr–BR metric, the leading magnetic modification enters through terms scaling as  $\sim B^2 r^2$ , such as in the conformal factor  $\Lambda = 1 + B^2 r^2$ . This dependence introduces a fundamental asymmetry in how the magnetic field affects orbits at different radii. The factor  $B^2 r^2$  acts as a confining geometrical contribution: for orbits at larger radii this term is significantly larger, implying that the magnetic field produces a stronger effective radial steepening of the potential than it does near the black hole.

To maintain a stable circular orbit against this enhanced radial confinement, the test particle requires a higher angular velocity to provide sufficient centrifugal support. This leads to a differential sensitivity of the frequency to  $B$  depending on the ISCO location. Prograde orbits, residing deep in the gravitational potential well ( $r_{\text{ISCO}} \approx 2m$ ), experience relatively modest magnetic corrections because  $B^2 r^2$  remains small. In

contrast, retrograde orbits are located much farther out ( $r_{\text{ISCO}} \approx 9m$ ), where the factor  $B^2r^2$  is more than an order of magnitude larger. Consequently, retrograde orbits are subject to a much stronger magnetic confinement effect, forcing a drastic increase in their orbital frequency. This enhanced sensitivity ( $\partial\Omega_{\text{ISCO}}/\partial B$ ) allows them to rapidly “catch up” and eventually overtake the less sensitive prograde orbits, resulting in the observed frequency crossover.

### C. Global parameter-space trends

To obtain a more global picture of the magnetic imprint, we extend our analysis to the entire spin interval  $a \in (-1, 1)$ . Figure 4 summarizes the interplay between the black hole’s intrinsic angular momentum and the external magnetic field.

We first focus on the frequency behavior shown in the right panel of Fig. 4. The red shaded region highlights a generic “magnetic hardening” of the gravitational-wave spectrum: for any given spin  $a$ , the magnetized ISCO frequency (red solid line) is higher than the corresponding vacuum value (black dashed line). The separation between the two curves becomes increasingly pronounced in the retrograde regime ( $a < 0$ ), whereas they tend to merge for rapidly spinning prograde orbits ( $a \rightarrow 1$ ). This behavior confirms that retrograde orbits act as hypersensitive probes of environmental magnetic fields, as the magnetic confinement effect dominates over the comparatively weaker gravitational binding at larger radii.

The left panel of Fig. 4 displays the corresponding shift in the ISCO radius. While the magnetic field invariably pushes the ISCO outward ( $r_{\text{mag}} > r_{\text{vac}}$ ), the magnitude of this shift exhibits a subtle, nonmonotonic dependence on spin, as detailed in the inset. Notably, the absolute deviation  $\Delta r_{\text{ISCO}} = r_{\text{mag}} - r_{\text{vac}}$  does not peak at the maximally retrograde spin ( $a = -1$ ), as one might naively expect from the large orbital radius alone. Instead, the maximum deviation occurs at an intermediate retrograde spin, approximately  $a \approx -0.26$ .

This nonmonotonic behavior can be qualitatively understood as the outcome of two competing physical mechanisms. First, as  $a$  becomes more retrograde, the ISCO radius  $r$  increases. Since the magnetic metric corrections scale as  $\sim B^2r^2$ , larger radii provide a longer “magnetic lever arm” to destabilize the orbit, tending to increase  $\Delta r_{\text{ISCO}}$ . Second, as  $a \rightarrow -1$ , the counter-rotating frame-dragging effects become dominant, creating a “stiffer” effective potential well. In this regime, the ISCO location is strongly dictated by the background spacetime geometry, making it increasingly resistant to external magnetic perturbations. The peak at  $a \approx -0.26$  therefore represents a balance point between the growing magnetic leverage and the increasing rigidity of the underlying gravitational potential.

## V. IMPRINT ON GRAVITATIONAL WAVES

To characterize the imprint of the magnetic field on gravitational waves, we adopt a relativistic adiabatic evolution scheme. In this framework, the conservative sector of the dynamics is governed by the exact geodesic motion in the Kerr-BR metric, so that the nonperturbative effects of the magnetic field on the spacetime geometry are fully retained. The resulting inspiral trajectories provide a direct bridge between the exact mathematical solution and astrophysical observables.

### A. Geodesic-driven inspiral evolution

We model the inspiral phase under the adiabatic approximation, assuming that the radiation-reaction timescale is much longer than the orbital period ( $T_{\text{rad}} \gg T_{\text{orb}}$ ). The trajectory of the compact object is then determined by the energy-balance equation

$$\frac{d\mathcal{E}_{\text{orbit}}}{dt} = -\dot{E}_{\text{GW}}.$$

To maximize the fidelity of the orbital motion, we treat the conservative and dissipative sectors with different levels of approximation. For the conservative sector, we use the *exact analytical expressions* for the specific energy  $\mathcal{E}(r; B)$  and orbital frequency  $\Omega_\phi(r; B)$  derived in Sec. III. This ensures that the orbital kinematics fully reflect the magnetically distorted geometry, without invoking weak-field or slow-motion expansions. For the dissipative sector, we employ the leading-order relativistic quadrupole formula for the gravitational-wave energy flux,

$$\dot{E}_{\text{GW}} = \frac{32}{5} \eta (m\Omega_\phi(r; B))^{10/3}, \quad (12)$$

where  $\eta = \mu/m \ll 1$  is the symmetric mass ratio.

Although the flux expression is approximate, evaluating it at the magnetically modified frequency  $\Omega_\phi(r; B)$  captures the dominant imprint of the background spacetime on the energy-loss rate. The evolution of the orbital radius is then obtained from

$$\frac{dr}{dt} = \frac{dr}{d\mathcal{E}} \frac{d\mathcal{E}}{dt} = -\left(\frac{\partial\mathcal{E}(r; B)}{\partial r}\right)^{-1} \dot{E}_{\text{GW}}. \quad (13)$$

Here, the radial derivative  $\partial\mathcal{E}/\partial r$  is computed *symbolically* from the metric components [Eqs. (5)] rather than by finite differencing, in order to avoid numerical inaccuracies near the ISCO where the potential gradient becomes small.

### B. Mechanism of accelerated inspiral

The physical mechanism responsible for the accelerated evolution is illustrated in Fig. 5, which disentangles

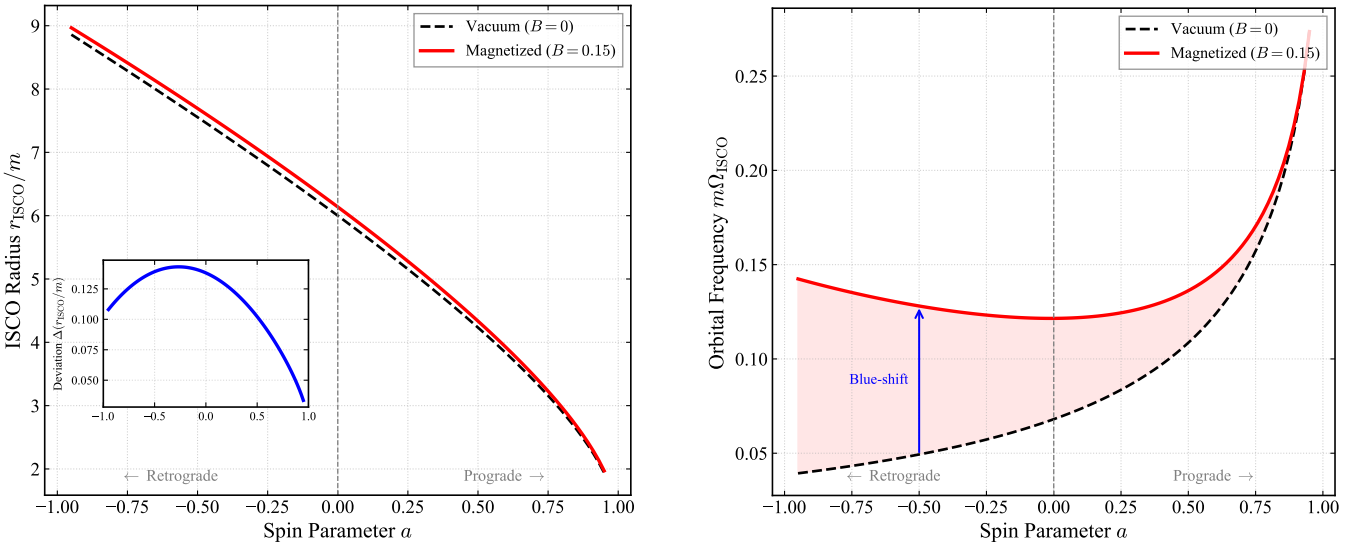


FIG. 4. **Global parameter-space scan.** Left: ISCO radius versus spin  $a$  for vacuum (black) and magnetized (red,  $B = 0.15$ ) cases. The inset highlights the absolute deviation  $\Delta r_{\text{ISCO}}/m$ , revealing a nonmonotonic sensitivity that peaks at  $a \approx -0.26$ . Right: ISCO frequency versus spin. The red shaded region represents the magnetic hardening (blue-shift) induced by the field, which is most significant for retrograde orbits.

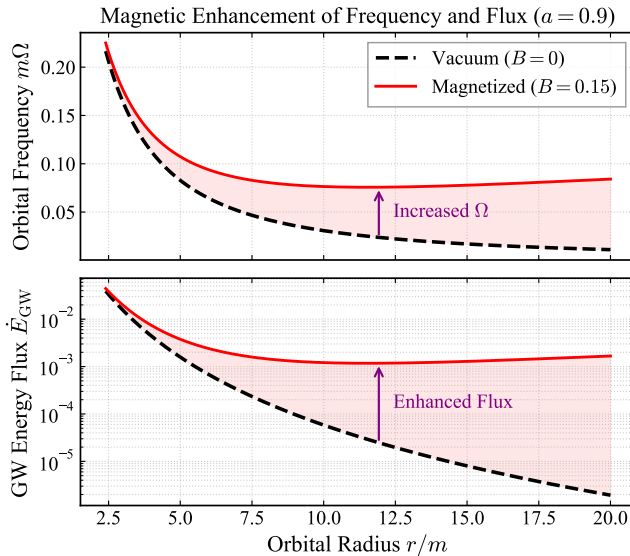


FIG. 5. **Magnetic enhancement of frequency and flux** ( $a = 0.9$ ). *Top:* The magnetic field modifies the radial potential and requires a higher orbital frequency  $\Omega_\phi$  to maintain circular orbits at a fixed radius. *Bottom:* Due to the steep frequency dependence of the gravitational-wave emission ( $\dot{E}_{\text{GW}} \propto \Omega_\phi^{10/3}$ ), this moderate frequency shift translates into a dramatic enhancement of the energy flux, driving a significantly faster inspiral.

the conservative and dissipative contributions to the dynamics.

First, we consider the *dynamical response* of the orbit (top panel). In the Kerr-BR spacetime, the magnetic

field introduces geometrical confinement terms that scale schematically as  $\sim B^2 r^2$  in the metric functions (e.g., through the conformal factor  $\Lambda = 1 + B^2 r^2$ ). These terms effectively steepen the radial potential well. To counteract this additional inward curvature and maintain a stable circular orbit at a fixed radius  $r$ , the test particle must possess a larger angular momentum and angular velocity than in the vacuum Kerr case. This leads to the frequency “blue-shift”  $\Omega_{\text{mag}} > \Omega_{\text{vac}}$  across the inspiral.

Second, we examine the *radiative consequence* (bottom panel). In the weak-field limit, the gravitational-wave energy flux scales as  $\dot{E}_{\text{GW}} \propto \Omega_\phi^{10/3}$ . This high-power dependence acts as a nonlinear amplifier: even a modest magnetic correction to the orbital frequency produces a substantial enhancement in the energy-emission rate. As shown in the logarithmic scale of Fig. 5 (bottom), the flux enhancement can reach orders of magnitude, depending on the field strength and orbital separation.

This “magnetic amplification” generates a feedback loop: the particle radiates energy more efficiently, causing the orbital radius to shrink more rapidly  $|dr/dt| \propto \dot{E}_{\text{GW}}$ , which in turn drives the system deeper into the strong-field region where the magnetic curvature corrections are even more pronounced. As a result, the magnetized system undergoes an accelerated inspiral and reaches the plunge significantly earlier than a vacuum system with identical initial parameters.

### C. Waveform dephasing and cutoff

We construct a time-domain gravitational-wave strain  $h(t)$  using a quadrupole proxy for the dominant (2, 2)

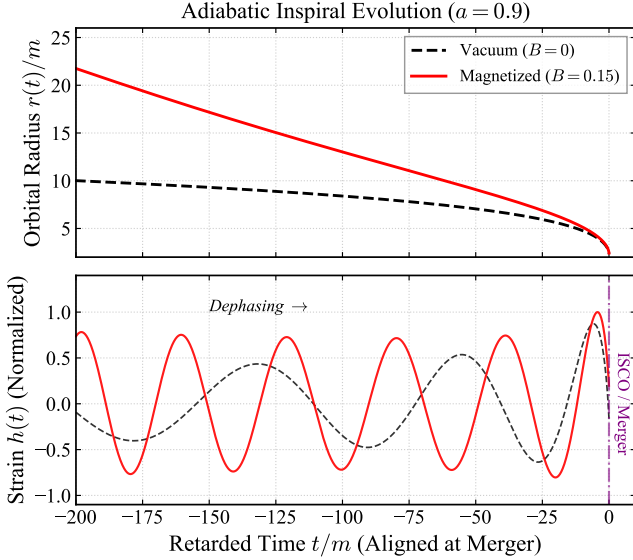


FIG. 6. **Waveform dephasing.** *Top:* Orbital radius evolution  $r(t)$ . The magnetized orbit ( $B = 0.15$ , red dashed) inspirals significantly faster than the vacuum case (black solid) due to the enhanced radiation flux. *Bottom:* Corresponding gravitational-wave strains. A large phase difference (dephasing) accumulates over the inspiral history. The vertical line at  $t = 0$  marks the ISCO/plunge, where the magnetized waveform terminates at a higher cutoff frequency than the vacuum waveform.

mode and an optimally oriented observer:

$$h(t) \propto (m\Omega_\phi(t))^{2/3} \cos \left[ 2 \int_0^t \Omega_\phi(t') dt' \right]. \quad (14)$$

The evolution is terminated when the particle reaches the ISCO ( $r(t) = r_{\text{ISCO}}$ ). We align the waveforms at the end of the inspiral (taken as  $t = 0$ ) to isolate the cumulative phase differences.

The resulting waveforms for a high-spin black hole ( $a = 0.9$ ) are shown in Fig. 6. The comparison between the vacuum (black solid) and magnetized (red dashed) cases reveals two main observational features.

First, the modified frequency evolution  $\dot{\Omega}_\phi(t)$  in the magnetized background leads to a substantial accumulated phase difference relative to the vacuum case. This dephasing becomes appreciable well before the plunge and, in principle, could be detectable in long-duration space-based observations.

Second, in line with the ISCO analysis of Sec. IV, the magnetized waveform extends to a higher orbital frequency before the plunge. This blue-shifted cutoff frequency constitutes a distinctive spectral feature of the magnetized environment, complementary to the cumulative dephasing in the inspiral phase.

It is worth noting the robustness of these results against model approximations. Although we employ a leading-order quadrupole flux, the dominant magnetic signature enters through the exact conservative dynam-

ics—specifically, the shifted orbital frequency  $\Omega_\phi(r)$ . By analogy with vacuum Kerr studies, higher-order relativistic corrections to the flux are expected to modify the absolute dephasing by only  $\mathcal{O}(10\%)$ , without altering the qualitative “blue-shift” trend. Given that the phase difference accumulated in Fig. 6 already exceeds tens of radians—well above the  $\mathcal{O}(1)$ -radian sensitivity threshold of LISA-like detectors—the magnetic dephasing remains a robustly observable effect.

## VI. CONCLUSION

In this work, we have investigated the orbital dynamics and gravitational-wave signatures of extreme mass-ratio inspirals (EMRIs) in the Kerr–Bertotti–Robinson spacetime. By implementing a semi-analytic adiabatic evolution scheme driven by exact geodesic relations, we quantified the imprint of an asymptotically uniform magnetic field on the binary evolution. Our analysis complements previous mathematical studies of exact type-D solutions [1, 32] by specifically exploring their implications for gravitational-wave astronomy, and reveals three main physical effects.

First, we find a robust “magnetic hardening” of the gravitational-wave spectrum. Although the magnetic field pushes the ISCO to larger radii ( $r_{\text{ISCO}}$  increases), it simultaneously introduces geometrical confinement that requires higher orbital frequencies for circular stability. As a result, the gravitational-wave cutoff frequency is systematically blue-shifted relative to the vacuum Kerr case. This counterintuitive behavior contrasts with the standard Newtonian expectation, in which radial expansion typically implies a frequency redshift.

Second, our global parameter-space scan highlights the hypersensitivity of retrograde orbits to environmental magnetic fields. We observe distinct frequency crossover phenomena; for instance, above a characteristic field strength ( $B \gtrsim 0.12$  in our examples), the ISCO frequency of a counter-rotating orbit can exceed that of a nonspinning Schwarzschild black hole. This demonstrates that sufficiently strong magnetic fields can modify—or even invert—the usual spin–frequency hierarchy at the ISCO. In a data-analysis context, such effects may break or induce parameter degeneracies in gravitational-wave observations. Neglecting magnetic corrections in waveform models could therefore introduce non-negligible biases, particularly in the inferred spin of the central black hole.

Finally, these dynamical modifications manifest as substantial dephasing in the time-domain waveform. The magnetic enhancement of the orbital frequency leads to a pronounced increase in the gravitational-wave energy flux ( $\dot{E}_{\text{GW}} \propto \Omega_\phi^{10/3}$ ), driving an accelerated inspiral. The resulting accumulated phase difference, together with the blue-shifted cutoff frequency at plunge, constitutes a characteristic signature for future space-based detectors such as LISA, TianQin, and Taiji.

While the present analysis provides a relativistic de-

scription of the inspiral phase within the adiabatic approximation, a comprehensive waveform template will also require modeling the merger and ringdown stages. A natural next step is to investigate quasinormal modes and perturbations in the Kerr–BR background, enabling a consistent description of the full coalescence signal in

the presence of large-scale magnetic fields.

## ACKNOWLEDGMENTS

This work was supported by the National Natural Science Foundation of China under Grant No. 12305070, and the Basic Research Program of Shanxi Province under Grant Nos. 202303021222018 and 202303021221033.

---

[1] J. Podolsky and H. Ovcharenko, Kerr Black Hole in a Uniform Bertotti-Robinson Magnetic Field: An Exact Solution, *Phys. Rev. Lett.* **135**, 181401 (2025), arXiv:2507.05199 [gr-qc].

[2] B. P. Abbott *et al.* (LIGO Scientific, Virgo), GWTC-1: A Gravitational-Wave Transient Catalog of Compact Binary Mergers Observed by LIGO and Virgo during the First and Second Observing Runs, *Phys. Rev. X* **9**, 031040 (2019), arXiv:1811.12907 [astro-ph.HE].

[3] R. Abbott *et al.* (LIGO Scientific, Virgo), GWTC-2: Compact Binary Coalescences Observed by LIGO and Virgo During the First Half of the Third Observing Run, *Phys. Rev. X* **11**, 021053 (2021), arXiv:2010.14527 [gr-qc].

[4] R. Abbott *et al.* (KAGRA, VIRGO, LIGO Scientific), GWTC-3: Compact Binary Coalescences Observed by LIGO and Virgo during the Second Part of the Third Observing Run, *Phys. Rev. X* **13**, 041039 (2023), arXiv:2111.03606 [gr-qc].

[5] Event Horizon Telescope Collaboration, First M87 Event Horizon Telescope Results. I. The Shadow of the Supermassive Black Hole, *Astrophys. J. Lett.* **875**, L1 (2019).

[6] Event Horizon Telescope Collaboration, First Sagittarius A\* Event Horizon Telescope Results. I. The Shadow of the Supermassive Black Hole in the Center of the Milky Way, *Astrophys. J. Lett.* **930**, L12 (2022).

[7] R. P. Kerr, Gravitational field of a spinning mass as an example of algebraically special metrics, *Phys. Rev. Lett.* **11**, 237 (1963).

[8] V. V. Kiselev, Quintessence and black holes, *Class. Quant. Grav.* **20**, 1187 (2003), arXiv:gr-qc/0210040.

[9] X.-Q. Li, B. Chen, and L.-L. Xing, Charged Lovelock black holes in the presence of dark fluid with a nonlinear equation of state, *Eur. Phys. J. Plus* **135**, 175 (2020), arXiv:1905.08156 [gr-qc].

[10] X.-Q. Li, B. Chen, and L.-L. Xing, Black holes surrounded by modified Chaplygin gas in Lovelock theory of gravity, *Annals Phys.* **446**, 169125 (2022).

[11] X.-Q. Li, H.-P. Yan, L.-L. Xing, and S.-W. Zhou, Critical behavior of AdS black holes surrounded by dark fluid with Chaplygin-like equation of state, *Phys. Rev. D* **107**, 104055 (2023), arXiv:2305.03028 [gr-qc].

[12] P. S. Letelier, Clouds of strings in general relativity, *Phys. Rev. D* **20**, 1294 (1979).

[13] M. Barriola and A. Vilenkin, Gravitational Field of a Global Monopole, *Phys. Rev. Lett.* **63**, 341 (1989).

[14] S. L. Detweiler, Klein-Gordon equation and rotating black holes, *Phys. Rev. D* **22**, 2323 (1980).

[15] T. J. M. Zouros and D. M. Eardley, Instabilities of massive scalar perturbations of a rotating black hole, *Annals Phys.* **118**, 139 (1979).

[16] M. A. Melvin, Pure magnetic and electric geons, *Phys. Lett.* **8**, 65 (1964).

[17] F. J. Ernst and W. J. Wild, Kerr black holes in a magnetic universe, *J. Math. Phys.* **17**, 182 (1976).

[18] R. M. Wald, Black hole in a uniform magnetic field, *Phys. Rev. D* **10**, 1680 (1974).

[19] J. Podolsky, Various metric forms of all type D black holes and their application, in *24th International Conference on General Relativity and Gravitation (GR24) and 16th Edoardo Amaldi Conference on Gravitational Waves (Amaldi16)* (2025) arXiv:2511.01029 [gr-qc].

[20] H. Ovcharenko and J. Podolsky, A novel class of rotating black holes with non-aligned electromagnetic field, in *24th International Conference on General Relativity and Gravitation (GR24) and 16th Edoardo Amaldi Conference on Gravitational Waves (Amaldi16)* (2025) arXiv:2511.04840 [gr-qc].

[21] F. Gray, D. Kubiznak, H. Ovcharenko, and J. Podolsky, Hidden symmetries and separability structures of Ovcharenko-Podolský and conformal-to-Carter space-times, (2025), arXiv:2511.21538, arXiv:2511.21538 [gr-qc].

[22] X. Wang, Y. Hou, X. Wan, M. Guo, and B. Chen, Geodesics and Shadows in the Kerr-Bertotti-Robinson Black Hole Spacetime, (2025), arXiv:2510.07914, arXiv:2507.22494 [gr-qc].

[23] H. Ali and S. G. Ghosh, Parameter Estimation of Magnetised Kerr Black Holes Using Their Shadows, (2025), arXiv:2508.15862, arXiv:2508.15862 [gr-qc].

[24] X.-X. Zeng, C.-Y. Yang, and H. Yu, Optical characteristics of the Kerr–Bertotti–Robinson black hole, *Eur. Phys. J. C* **85**, 1242 (2025), arXiv:2508.03020 [gr-qc].

[25] A. Vachher, A. Kumar, and S. G. Ghosh, The influence of uniform magnetic fields on strong field gravitational lensing by Kerr black holes, *JCAP* **2025** (11), 021, arXiv:2508.21100 [gr-qc].

[26] X.-X. Zeng and K. Wang, Energy extraction from the Kerr-Bertotti-Robinson black hole via magnetic reconnection in a circular and a plunging plasma, *Phys. Rev. D* **112**, 064032 (2025), arXiv:2507.21777 [gr-qc].

[27] M. Astorino, Black holes in the external Bertotti-Robinson-Bonnor-Melvin electromagnetic field, *Phys. Rev. D* **112**, 104077 (2025), arXiv:2508.12908 [gr-qc].

[28] M. Ortaggio, Einstein-Maxwell fields as solutions of Einstein gravity coupled to conformally invariant non-linear electrodynamics, (2025), arXiv:2511.13665, arXiv:2511.13665 [gr-qc].

- [29] F. Ahmed, İ. Sakalli, and A. Al-Badawi, Kerr-Bertotti-Robinson Black Holes Surrounded by a Cloud of Strings, (2025), arXiv:2511.11792, arXiv:2511.11792 [gr-qc].
- [30] J. A. Rueda, R. Ruffini, and Y. Wang, Short GRB 090510: A magnetized neutron star binary merger leading to a black hole, JHEAp **50**, 100464 (2026), arXiv:2509.08172 [astro-ph.HE].
- [31] Y.-K. Zhang and S.-W. Wei, Effects of magnetic fields on spinning test particles orbiting Kerr-Bertotti-Robinson black holes, (2025), arXiv:2510.07914, arXiv:2510.07914 [gr-qc].
- [32] T. Wang, Innermost stable circular orbit of Kerr-Bertotti-Robinson black holes and inspirals from it: Exact solutions, (2025), arXiv:2508.04684, arXiv:2508.04684 [gr-qc].
- [33] S. Chandrasekhar, *The mathematical theory of black holes* (1985).